Journal of Catalysis 329 (2015) 10–21

Contents lists available at ScienceDirect

Journal of Catalysis

journal homepage: www.elsevier.com/locate/jcat

Toward rational design of stable, supported metal catalysts for aqueous-phase processing: Insights from the hydrogenation of levulinic acid

Omar Ali Abdelrahman [a], Helen Y. Luo [b], Andreas Heyden [c], Yuriy Román-Leshkov [b], Jesse Q. Bond [a,*]

[a] Department of Biomedical and Chemical Engineering, Syracuse University, Syracuse, NY 13244, USA
[b] Department of Chemical Engineering, Massachusetts Institute of Technology, Cambridge, MA 02139, USA
[c] Department of Chemical Engineering, University of South Carolina, Columbia, SC 29208, USA

ARTICLE INFO

Article history:
Received 9 February 2015
Revised 18 April 2015
Accepted 21 April 2015

Keywords:
Aqueous-phase stability
Support effect
Levulinic acid
Ketone hydrogenation
Sintering
Ruthenium
γ-valerolactone

ABSTRACT

Aqueous-phase hydrogenation of levulinic acid (4-oxopentanoic acid) and 2-pentanone was considered to probe the activity and stability of supported Ru catalysts during ketone hydrogenation in water. Selected supports include activated carbon, amorphous SiO_2, γ-Al_2O_3, and TiO_2. For both probe molecules, intrinsic hydrogenation activity was independent of support identity and Ru particle size. Moreover, the presence of a secondary functional group in levulinic acid (i.e., a carboxyl group) and the resulting dissociated protons do not appear to perturb the activity of Ru sites in water. LA hydrogenation thus appears kinetically equivalent to that of 2-pentanone, and both occur with an average turnover frequency of 0.11 s^{-1} under our experimental conditions (323 K, 24 bar H_2, 0.5 M LA/2-Pentanone). Supported Ru clusters were susceptible to both irreversible and reversible modes of deactivation. The former was attributed to particle sintering, which is accelerated in bulk water relative to gas phases. The extent of particle growth is relatively insensitive to solution pH and depends primarily on the nature of the support, decreasing in the order $SiO_2 > C \approx TiO_2 >$ γ-Al_2O_3. Reversible activity losses are also support-dependent; however, the underlying cause could not be identified conclusively. Its extent correlates with the dominant surface charge of the support under experimental conditions. As such, trends in reversible and irreversible deactivation both appear to be governed by the bulk electronegativity of the support.

1. Introduction

Development of efficient strategies for the production of industrial commodities from non-petroleum resources is a long-standing goal of catalysis research. The catalytic challenges inherent in any such strategy reflect both the nature of the feedstock and the intent of upgrading. For example, selective methane functionalization is hindered by the stability of the feedstock (methane) relative to its intended products (e.g., methanol). In contrast, during biomass processing, one works with oxygenated feedstocks and is typically interested in reducing their functionality to approximate petroleum refinery products. With the exception of gasification, biomass deconstruction will generally yield intermediate chemicals that are characterized by low vapor pressure and high reactivity. In contrast to petroleum upgrading, biomass and its derivatives are best suited to low temperature, condensed-phase processing. More specifically, since biomass has a high water content, and bio-derived commodities are often oxygen-rich, many upgrading strategies are expected to occur in aqueous media.

A number of catalytic technologies have been explored for converting biomass and its derivative platforms into energy-dense fuels and value-added chemicals. Aqueous-phase reforming allows the production of H_2 and/or syngas directly from carbohydrates [1,2]; decarbonylation and decarboxylation of carboxylic acids deliver alkenes and alkanes [3–7]; and hydrodeoxygenation facilitates selective cleavage of C–O bonds to form fully reduced alkanes that retain the entire carbon content of the parent feedstock (i.e., they occur without C–C cleavage) [8–11]. A common characteristic of the above is that each requires metal catalysts in some capacity.

Abbreviations: LA, levulinic acid; GVL, γ-valerolactone; HPA, 4-hydroxypentanoic acid.

* Corresponding author at: Department of Biomedical and Chemical Engineering, 329 Link Hall, Syracuse University, Syracuse, NY 13244, USA.
E-mail address: jqbond@syr.edu (J.Q. Bond).

http://dx.doi.org/10.1016/j.jcat.2015.04.026
0021-9517/

Aqueous-phase reforming employs metal sites to facilitate dehydrogenation, C–C cleavage, and water–gas shift [1,2,12–15]; and metal surfaces similarly activate carboxylic acids for decarboxylation and decarbonylation [3,7]. Although HDO strategies leverage acid sites to cleave C–O bonds through dehydration, extensive reduction in oxygen content—as required for biofuel production—inevitably requires H_2 addition and suggests complementary use of metal catalysts [8–10]. Similarly, processes such as transfer hydrogenation for carbonyl reduction, which can be catalyzed by Lewis acidic solid oxides [16–19], require reduced metal sites in ancillary roles [20].

In light of the above points, it is no surprise that the biomass processing literature is rich with examples of technologies that employ supported metal catalysts in aqueous media [1,12–15,21–31]. Unfortunately, metal catalysts are relatively expensive, and their price contributes significantly to the (present) high cost of bio-based commodities [32]. To minimize catalyst expenses where metals are employed, they must provide intrinsically high activity and offer stable onstream performance. While the former is frequently demonstrated, the latter remains elusive. Aqueous media and high temperatures can expedite catalyst deactivation; furthermore, mineral and organic acids are commonly encountered in biomass processing, and many applications additionally demand that metal catalysts perform stably at low pH [3,33–37]. The severity of the aqueous phase—and its effect on catalyst stability—has been frequently considered, and prior discussion has largely centered on support hydrothermal stability [38–42]. Given that carbon is relatively impervious to hydrolysis, it has emerged as a favored support for aqueous-phase applications. However, while support stability is necessary for catalyst stability, it is not sufficient to guarantee catalyst stability. For example, Ru/C is a popular catalyst choice for carbonyl hydrogenation; however, we recently observed that, despite retention of support integrity, it undergoes pronounced deactivation during aqueous-phase hydrogenation of the ketone group in bifunctional levulinic acid (LA, 4-oxopentanoic acid), even under relatively mild conditions (323 K, 0.5 M LA, pH = 2.45) [21]. A portion of the observed deactivation was irreversible and attributed to particle sintering, while a secondary deactivation mechanism appeared largely reversible. These observations are qualitatively consistent with prior accounts of Ru deactivation in related systems, and it is broadly acknowledged that improving the stability of Ru-based catalysts could improve the economic viability of γ-valerolactone production from biomass resources. From an applied standpoint, bimetallic formulations appear to offer enhanced stability during LA hydrogenation [31,43,44]; however, the mechanism by which promoter metals prevent Ru deactivation is unclear. Much of this uncertainty—and hence our ability to rationally design hydrogenation catalysts that offer stable performance in water—stems from a poor understanding of the phenomena that govern metal deactivation in such systems. Accordingly, the present study further considers the reversible and irreversible modes of deactivation that affect supported Ru catalysts during aqueous-phase ketone hydrogenation. It additionally correlates their severity with fundamental properties of the catalyst and the media in which it is employed. Through consideration of both LA and 2-pentanone hydrogenation over Ru supported on SiO_2, γ-Al_2O_3, TiO_2, and C, we highlight the influence of support identity and solution pH on the intrinsic activity and stability of Ru surface sites during aqueous-phase ketone hydrogenation. Although the hydrothermal stability of solid oxides is generally poor compared to carbon, they provide us with relatively well-defined model surfaces, and their consideration alongside carbon should aid in mapping design criteria that allow stabilization of supported metals in aqueous, acidic media.

2. Experimental

2.1. Materials and methods

Levulinic acid (LA, 98%, Sigma Aldrich), γ-valerolactone (GVL, 98%, Sigma Aldrich), 2-pentanone (99%, Acros Organics), 2-pentanol (DL, 98%, Acros Organics), propanoic acid (99%, Acros Organics), and sulfuric acid (95–98 wt%, Sigma Aldrich) were used in kinetic studies, standard preparation, and liquid chromatography. Catalyst syntheses employed ruthenium (III) chloride hexahydrate (35–40% Ru, Acros Organics), amorphous SiO_2 (481 m^2/g, Sigma Aldrich), γ-Al_2O_3 (231 m^2/g, Strem Chemicals) and TiO_2 (Aeroxide© P25, 55 m^2/g, Acros Organics). Commercial 0.5 wt% Ru/C and 5 wt% Ru/C samples were purchased from Strem Chemicals. H_2 (99.999%, Airgas), N_2 (99.999%, Airgas), and CO (99.99% Praxair) were employed in kinetic studies, catalyst pretreatment, and catalyst characterization. All above reagents were used as supplied by the manufacturer. Water used in the preparation of catalysts, reactor feeds, calibration standards, and HPLC mobile phases was purified in house by sequential reverse osmosis, UV oxidation, and double ion exchange.

2.2. Catalyst preparation

Catalysts comprised of Ru supported on γ-Al_2O_3, SiO_2, and TiO_2 were prepared via incipient wetness impregnation of the desired support with aqueous ruthenium (III) chloride hexahydrate. Impregnated catalysts were dried in air at 393 K and subsequently reduced in flowing H_2 (100 ml min^{-1}, 673 K, 3 K min^{-1}). Prior to removal from reduction vessels, samples were passivated at 298 K in a stream of 1% O_2 in He.

2.3. Catalyst characterization

Catalyst surface area and porosity were probed by N_2 physisorption at 77 K (Micromeritics ASAP 2020). Before N_2 dosing, samples were outgassed under vacuum (6 h, 623 K). Total surface areas and pore size distributions were obtained through BET and BJH analyses of the N_2 adsorption/desorption isotherm. Pore volumes were estimated from the total N_2 uptake at a relative pressure of 0.995.

Ru surface sites were quantified by adsorption of CO at 308 K (Micromeritics ASAP 2020). Prior to dosing, samples were reduced in flowing H_2 (3 h, 673 K, 3 K min^{-1}), evacuated at 673 K for 1 h to remove chemisorbed hydrogen, and cooled to 308 K under vacuum. Analysis was then performed at 308 K by collecting an adsorption isotherm, evacuating the sample for 1 h to remove physisorbed CO, and collecting a second isotherm. Irreversible CO adsorption was determined from the difference in CO adsorption between the first and second isotherms. Here, irreversible CO uptake was taken as equivalent to the Ru surface site density, which assumes a CO adsorption stoichiometry of 1. Surface-averaged Ru particle diameters based on irreversible CO uptake were calculated according to Eq. (1), which assumes a spherical morphology:

$$d_{p,CO} = \frac{6}{S \cdot \rho_{Ru}} \tag{1}$$

where S is the surface area of Ru per gram of catalyst calculated from irreversible CO uptake and ρ_{Ru} is the density of metallic Ru. The cross-sectional area of a single Ru atom was assumed to be 6.14 $Å^2$, and 12.30 g cm^{-3} was used as the density of Ru [45].

2.4. TEM

Average Ru cluster sizes and particle size distributions were determined using transmission electron microscopy (TEM). Catalyst samples were suspended in excess acetone via sonication, and suspension aliquots were deposited on 300 mesh carbon film Cu grids (EMS) and dried overnight under ambient conditions. Images were taken using a JEOL 2010F equipped with a Schottky field emission gun operating at 200 kV and captured with a CCD camera. Particle size distributions were extracted from TEM images using image processing software (ImageJ). Average particle sizes reported here represent the surface-averaged diameter, which is calculated according to Eq. (2) [46]:

$$d_{p,TEM} = \frac{\sum_i n_i \cdot d_i^3}{\sum_i n_i \cdot d_i^2} \quad (2)$$

In Eq. (2), d_i represents the mean of a specified range of particle diameters, n_i represents the number of particles within that range, and $d_{p,TEM}$ is the average particle size. Standard deviations for the surface-averaged diameter were calculated according to Eq. (3) [46]:

$$\sigma = \sqrt{\frac{\sum_i n_i d_i^2 (d_i - d_{p,TEM})^2}{\sum_i n_i d_i^2}} \quad (3)$$

2.5. Catalytic activity testing

Aqueous-phase hydrogenations were carried out in an upflow, packed bed reactor that has been described elsewhere [21]. Reactor feeds were prepared by dissolving levulinic acid (0.5 M) or 2-pentanone (0.5 M) in double deionized water, and catalysts were reduced in situ under flowing H_2 (673 K, 4 h, 3 K min^{-1}) prior to feed introduction. The liquid effluent was collected in a vapor–liquid separator and analyzed offline. LA and its hydrogenation products, 4-hydroxypentanoic acid (HPA) and GVL, were quantified using high-performance liquid chromatography (HPLC, Agilent 1100) by eluting reactor samples through an Agilent Hi-Plex H column with a 5 mM aqueous H_2SO_4 mobile phase. Analyte concentrations were determined using a variable wavelength detector operating at 195 nm. Cyclization of HPA to form GVL is both thermodynamically favorable and relatively facile. A portion of the HPA present in reaction products always forms GVL under our analysis conditions, which complicates an explicit determination of HPA/GVL selectivity. We have previously reported upon resolution of both HPA and GVL in reaction media [21]; however, our discussion here only requires estimating the total rate of LA (ketone) hydrogenation. This can be reliably obtained from the sum of HPA and GVL production rates, which are independent of the precise HPA/GVL distribution. 2-pentanone and its hydrogenation product, 2-pentanol, were quantified by GC-FID (Agilent 7890) using an HP-Innowax column (Agilent). This analytical approach led to >95% closure of carbon balances. For all reported experiments, reactors were operated under conditions that have been previously demonstrated to be free of mass transfer limitations during levulinic acid hydrogenation over 5 wt% Ru/C [21]. Though we have not exhaustively investigated diffusion limitations in this study, all catalysts tested have porosities, areal Ru site densities, and volumetric ketone hydrogenation rates that are—with respect to transport limitations—comparable to or more favorable than 5 wt% Ru/C. We thus assume that data reported here represent kinetically controlled hydrogenation rates.

This study focuses on the activity and onstream stability of supported Ru during the aqueous-phase hydrogenation of LA and 2-pentanone. The chemistry of interest in each case is hydrogenation of a ketone functional group; accordingly, our discussion emphasizes rates of ketone hydrogenation. To allow meaningful comparisons among catalysts having varied supports and metal loadings, hydrogenation rates are reported on a per-site basis as the total site-time yield (STY) of hydrogenation products:

$$\mathrm{STY}_i = \frac{\sum_j F_j}{S_{R_i}} \quad (4)$$

In Eq. (4), F_j is the molar flowrate of an individual hydrogenation product, and S_R is the total molar quantity of Ru surface sites in a given catalyst bed. For LA, the hydrogenation STY reflects the sum of HPA and GVL production per Ru surface site [21]. For 2-pentanone, it is based only on the rate of 2-pentanol production. Catalysts in all experiments deactivate with time on stream. To allow correlation with ex situ methods of site titration, hydrogenation rates are reported as initial rates, which were estimated by extrapolation of deactivation profiles to zero time on stream [21].

To probe the reversibility of deactivation, aqueous feeds were periodically interrupted, and catalysts were reduced in situ under flowing H_2 (100 ml min^{-1}, 1 bar). For most samples, reduction was carried out at 673 K as discussed in the catalyst preparation section; however, regeneration at this temperature induced anomalous, irreversible deactivation in Ru/TiO_2. As such, Ru/TiO_2 was regenerated at 323 K. Spent catalysts were recovered for characterization after drying in situ under N_2 (90 ml min^{-1}, 3 h, 573 K, 1 K min^{-1}).

3. Results

3.1. Catalyst activity

Table 1 summarizes physical and chemical characteristics of the supported Ru catalysts considered in this study. Our intent was to compare, as closely as possible, catalysts having similar Ru dispersions and particle sizes, and most considered here were prepared at comparable areal Ru loadings to a previously studied catalyst, Ru/C-A (Entry 1) [21]. 0.5 wt% Ru/C and 0.3 wt% Ru/SiO_2 samples were additionally included in an attempt to extend the range of particle sizes considered on these supports. Where possible, particle sizes were determined by both CO chemisorption and TEM. Results of the two methods generally agree, revealing that that initial Ru particle sizes are within the range of 1–4 nm for all samples. Based on its CO adsorption capacity, the particle diameter for Ru/C-B appears overestimated by TEM, and we consider CO uptake to provide the more reliable estimate of initial cluster size for this sample (1.2 nm). Particle sizes vary with support and metal loading, which is anticipated according to prior reports employing impregnation methods for the preparation of supported Ru catalysts [47–49], and we account for this variation to the extent possible in subsequent analyses. CO uptakes from Table 1 provide the basis for calculation of site-time yields, and other properties are highlighted where relevant.

Table 2 summarizes site-time yields of ketone hydrogenation products observed during hydrogenation of LA (0.5 M, aq.) and 2-pentanone (0.5 M, aq.) over Ru supported on C, SiO_2, Al_2O_3, and TiO_2 at 323 K. Importantly, this presentation relies on-site-normalized hydrogenation rates, which correct for variations in metal dispersion and allow us to rigorously discuss the influence of particle size on rates of ketone hydrogenation in the aqueous phase. Excepting $Ru\text{-}SiO_2$-B, each catalyst was tested at both relatively high and relatively low space velocities. The former

Table 1
Physical and chemical properties of supported Ru catalysts employed in this study.

Sample	SA (m^2/g)	V_p (cm^3/g)	D_p (nm)[a]	Ru (wt.%)[b]	Ru (μmol/m^2)	CO uptake (μmol/g)	$d_{p,TEM}$ (nm)[c]	$d_{p,CO}$ (nm)[d]
Ru/C-A	756	0.70	5.1	5.0	0.65	220	4.0 ± 0.3	3.2
Ru/C-B	780	0.66	5.1	0.5	0.07	61	4.0 ± 0.3	1.2
Ru/SiO_2-A	468	0.82	5.5	2.7	0.57	116	2.7 ± 0.1	3.3
Ru/SiO_2-B	468	0.82	5.5	0.3	0.06	18	–	2.2
Ru/γ-Al_2O_3	230	0.44	5.7	1.3	0.56	105	1.7 ± 0.1	1.6
Ru/TiO_2	55	0.42	24.1	0.4	0.69	15	3.1 ± 0.3	3.3

[a] Average pore diameter determined by BJH analysis of N_2 adsorption/desorption data.
[b] Based upon concentrations of impregnating solutions, incipient volume, and support mass.
[c] Confidence intervals calculated at 95%.
[d] Estimated from CO chemisorption.

Table 2
Summary of initial rates of hydrogenation for both levulinic acid and 2-pentanone in bulk water at 323 K, 24 bar H_2, and 0.5 M dissolved organic. Conversions and rates are both reported at zero time on stream.

Entry	Sample	Feed	WHSV (g ketone g catalyst^{-1} h^{-1})	Conversion (%)	STY (s^{-1})[a]
1	Ru/C-A	LA	520	2	0.09 ± 0.028
2	Ru/C-A	LA	37	20	0.08 ± 0.011
3	Ru/C-B	LA	34	8	0.11 ± 0.009
4	Ru/C-B	LA	12	33	0.15 ± 0.011
5	Ru/SiO_2-A	LA	32	16	0.11 ± 0.019
6	Ru/SiO_2-A	LA	18	42	0.16 ± 0.007
7	Ru/SiO_2-B	LA	22	4	0.10 ± 0.012
8	Ru/Al_2O_3	LA	27	14	0.09 ± 0.007
9	Ru/Al_2O_3	LA	11	35	0.10 ± 0.005
10	Ru/TiO_2	LA	25	3	0.11 ± 0.015
11	Ru/TiO_2	LA	11	7	0.12 ± 0.014
12	Ru/SiO_2-A	2-pentanone	27	18	0.11 ± 0.021
13	Ru/SiO_2-A	2-pentanone	13	36	0.13 ± 0.004
14	Ru/Al_2O_3	2-pentanone	20	29	0.14 ± 0.010
15	Ru/Al_2O_3	2-pentanone	12	44	0.14 ± 0.010

[a] Confidence intervals calculated at 95%.

allowed estimation of site-time yields under conditions of low ketone conversion, and the latter ensured sufficient mass loadings to facilitate recovery and characterization of spent catalysts. For any given sample, one observes that hydrogenation STYs over Ru sites are, within the precision of our estimates, invariant with space velocity and ketone conversion. This result is consistent with prior observations that both gas- and liquid-phase ketone hydrogenations appear zero order in the ketone over the range of concentrations considered [50–52]. Moreover, no significant variation in (initial) site-time yield is observed between any two supports, suggesting that intrinsic rates of LA hydrogenation over Ru in water are not strongly affected by metal–support interactions. This result agrees with data reported by both Subramaniam and Rooney, which indicate comparable turnover frequencies during aqueous-phase hydrogenation of 2-butanone over Ru supported on C [53] and SiO_2 [54]. Finally, entries 12–15 indicate that rates of 2-pentanone hydrogenation are comparable to those of LA hydrogenation, allowing the conclusion that the secondary carboxylic acid functionality in LA and the resultant increase in aqueous proton concentrations do not strongly perturb the intrinsic ketone hydrogenation activity of Ru sites in water.

The initial rates summarized in Table 2 were obtained by extrapolation of decaying hydrogenation rates to zero time on stream, and some scatter in the data is inevitable. Despite this, Fig. 1 illustrates that, for all catalysts summarized in Table 1, mass-normalized hydrogenation rates during reduction of both 2-pentanone and LA are first order in Ru surface site density. Furthermore, both sets of data are captured by a single, linear correlation. This allows determination of an average STY for ketone hydrogenation via regression of hydrogenation rates as a function of site densities, and we estimate it to be 0.11 ± 0.016 s^{-1} under the reported conditions. It must be acknowledged that many of the

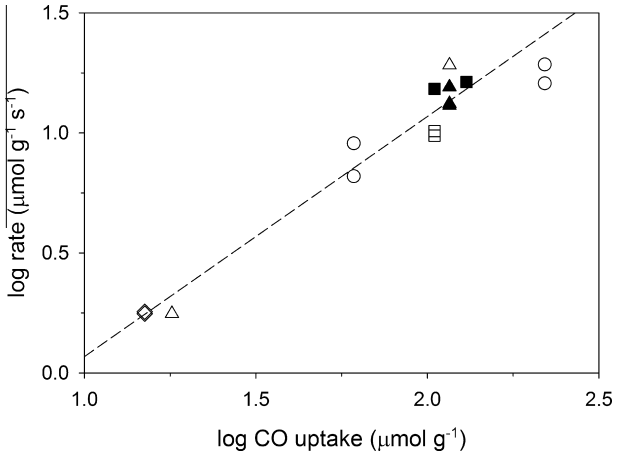

Fig. 1. Functional relationship between mass-normalized ketone hydrogenation rates and Ru surface site densities as determined by CO chemisorption. Hydrogenation rates were measured at 0.5 M ketone concentration at 323 K and 24 bar H_2. (◇) Ru/TiO_2, (○) Ru/C, (Δ) Ru/SiO_2, and (□) Ru/γ-Al_2O_3. Open symbols represent LA hydrogenation rates. Filled symbols represent 2-pentanone hydrogenation rates. The slope of the regression line indicated in the figure is 1.0 ± 0.14, which is consistent with criteria given by Koros and Nowak for demonstration of kinetically controlled hydrogenation rates at a given temperature.

hydrogenation rates illustrated in Fig. 1 were not obtained under conditions of differential ketone conversion; however, since hydrogenation rates appear zero order with respect to the ketone, site-time yields of hydrogenation products should be invariant with ketone conversion. Therefore, the average site-time yield measured here provides a reasonable estimate for the turnover frequency of both 2-pentanone and LA hydrogenation over Ru sites at

323 K and 24 bar H_2. A final consequence of the data shown in Fig. 1 is that, since one clearly observes a linear correlation between catalyst productivity and Ru site density, data are consistent with kinetically controlled hydrogenation rates for all samples considered [55,56]. Because initial metal dispersions varied in this study, Fig. 1 also suggests that Ru cluster sizes do not substantially affect turnover frequencies for ketone hydrogenation in the size range considered here (1–4 nm). Glucose hydrogenation on Ru [26] and acetone hydrogenation on Pt [51,52] are both reported to be structure independent; as such, our observation of structure insensitivity in this system is consistent with prior accounts of carbonyl hydrogenation over Group VIII metals.

3.2. Catalyst stability

We first consider the stability of Ru supported on SiO_2, γ-Al_2O_3, TiO_2, and C by examining their activity (a) with time on stream during LA hydrogenation (Fig. 2). Activity for each catalyst is defined as its measured rate of ketone hydrogenation at a given time on stream normalized by its estimated rate of hydrogenation at zero time on stream. Samples were subjected to periodic regeneration to determine the extent to which activity losses were reversible, and regeneration attempts are indicated by dashed vertical lines. Our standard regeneration procedure was to reduce catalyst samples in flowing H_2 at 673 K; however, this treatment was observed to substantially and irreversibly diminish hydrogenation rates of Ru/TiO_2. Though we cannot state so conclusively, this may be attributed to partial encapsulation of Ru particles by the reducible TiO_2 support during high-temperature regeneration [57,58]. We have observed that reduction at 323 K is sufficient to restore reversible deactivation of supported Ru catalysts in this system without inducing irreversible deactivation in Ru/TiO_2. Accordingly, we have employed this alternative protocol for regeneration of Ru/TiO_2.

Measured hydrogenation site-time yields in this system are relatively high (≈0.01–0.1 s^{-1}), and the volumetric residence time in each experiment is relatively small (≈10 min), suggesting that the system should approach steady state within an hour. Reference experiments carried out under steady state conditions confirmed that normally anticipated transient phenomena (e.g., those associated with system volume and/or transients in surface coverage) are complete within 15–20 min, whereas Fig. 2 illustrates that catalyst activity decays on the scale of hours. This indicates that catalyst deactivation underlies the observed transient phenomena.

Deactivation profiles in Fig. 2 reveal that supported Ru catalysts are susceptible to both reversible and irreversible activity losses during aqueous-phase hydrogenation of LA at 323 K; however, the extent of each deactivation pathway varies considerably in the catalysts tested. For example, activity lost by Ru/SiO_2 is entirely non-recoverable upon in situ reduction (Fig. 2a), whereas activity losses observed for Ru/γ-Al_2O_3 appear to be primarily reversible in nature (Fig 2b). Ru nanoparticles supported on TiO_2 and C undergo both types of deactivation to varying extents. Based on control experiments performed with Ru/γ-Al_2O_3, activity is only restored through treatment in H_2; catalyst regeneration was not possible in analogous treatments in He.

Before proceeding with further analysis of the two modes of instability, we highlight differences observed during aqueous-phase hydrogenation of LA and 2-pentanone (Fig. 3). For this comparison, Ru/SiO_2 and Ru/γ-Al_2O_3 were selected since these two catalysts displayed extreme differences in extents of reversible and irreversible activity losses during LA hydrogenation. Over Ru/SiO_2, there is no quantifiable difference in catalyst stability during aqueous-phase hydrogenation of 2-pentanone and LA (Fig. 3a). In both cases, deactivation is irreversible, and it occurs to comparable extents over 16 h on stream. In contrast, Ru/γ-Al_2O_3 is considerably more stable during 2-pentanone hydrogenation than it is during LA hydrogenation (Fig. 3b). Based on initial rates measured after each regeneration attempt, Ru/γ-Al_2O_3 appears to exhibit comparable irreversible deactivation in both cases, while the extent of reversible deactivation is greater during LA hydrogenation.

A number of phenomena can cause deactivation of supported metals, and the severity of any can be influenced by several factors including the nature of the metal, its interaction with the support, the size of metal clusters, operational parameters, and the environment in which the catalyst is employed. Considering the complexity of catalyst deactivation, direct comparison of the results summarized in Figs. 2 and 3 is difficult. In subsequent sections, we attempt to decouple the observed deactivation pathways and arrive at a set of principles that govern the stability of supported Ru catalysts during aqueous-phase ketone hydrogenation.

3.3. Irreversible deactivation

Table 3 summarizes physicochemical properties of spent catalysts, which were recovered from LA hydrogenation reactors after the period on stream indicated in Fig. 2. To facilitate comparison and correlation, analogous data are presented for each catalyst in a pristine state. The table further summarizes the percentage of activity irreversibly lost during the on stream period.

From the data in Table 3, it is evident that physical properties associated with support structure do not change significantly between fresh and spent catalysts, and no substantial perturbations in surface area and porosity are observed in any system. Although support hydrothermal stability is critical in aqueous-phase catalysis [39,41], support degradation does not appear to underlie irreversible deactivation in this study. X-ray diffraction patterns (online supporting information) do not show a significant change in support structure between pre- and post-reaction samples. Though not particularly meaningful for amorphous C and SiO_2, retention of initial diffraction patterns for γ-Al_2O_3 and TiO_2 indicates that phase changes, which are realistic for these materials in water [59,60], are sufficiently slow at 323 K that they are not observed over the reported times on stream.

Examining CO uptake in fresh and spent catalysts (Table 3), it is apparent that irreversible decreases in hydrogenation activity correlate with a decrease in CO uptake, which we take to indicate a loss of accessible Ru surface sites with time on stream. Previously, we analyzed reactor effluents from LA hydrogenation over 5 wt% Ru/C via ICP-MS, and we found no evidence of metal leaching [21]. This is consistent with multiple prior accounts describing the insolubility of zerovalent Ru in water [26,27,54,61]. We thus conclude that Ru leaching does not occur in the systems described here—at least not on scales commensurate with the observed activity losses. As such, irreversible activity losses are most likely attributed either to particle sintering or to irreversible site poisoning through binding of species that block CO uptake and cannot be removed by a reductive treatment (e.g., hard coke, metal ions). Irreversible poisoning is certainly realistic in this system. Data were obtained in stainless steel reactors under acidic conditions where dissolution of metal ions from reactor walls is possible and could contribute to catalyst deactivation. Further, carbon deposition can occur on metal surfaces [62]. Although we are not able to definitively exclude poisoning and coke formation as a potential causes, we believe that neither contributes significantly to the irreversible deactivation observed here. Specifically, data in Table 3 clearly indicate particle growth as the source of reduced CO uptake with time on stream. For all samples exhibiting irreversible deactivation, average Ru particle diameters are observed to increase via TEM. Moreover, Fig. 4 illustrates that normalized decreases in CO uptake between fresh and spent

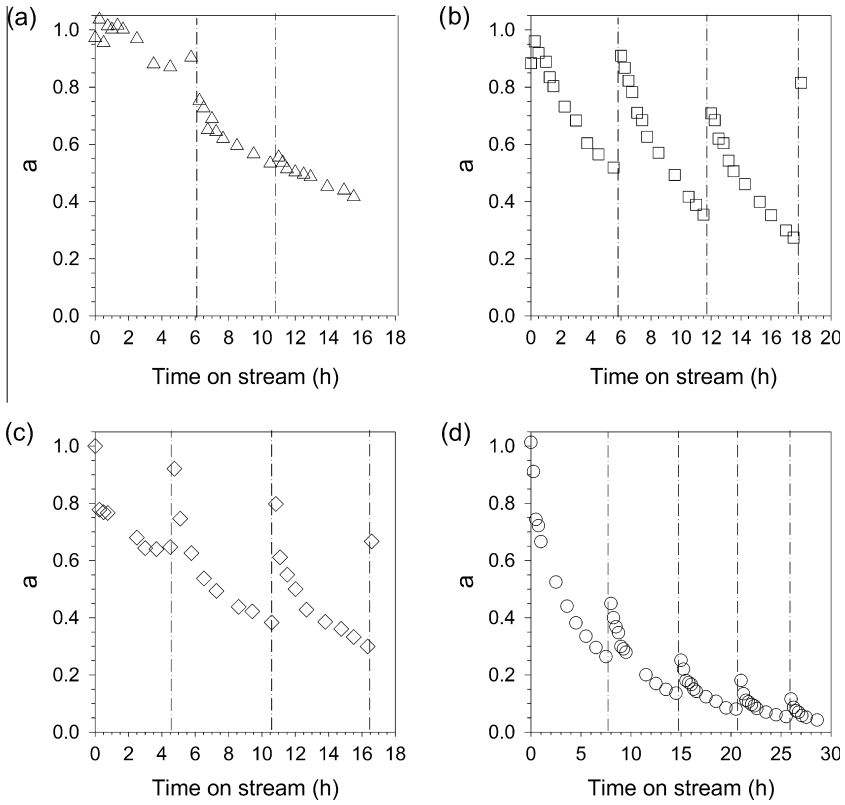

Fig. 2. LA hydrogenation activity as a function of time on stream for Ru supported on (a) 2.7 wt% on SiO_2, (b) 1.3 wt% on γ-Al_2O_3, (c) 0.4 wt% on TiO_2, and (d) 0.5 wt% on C. Observed deactivation profiles for samples prepared at different Ru loadings were qualitatively similar to the above trends such that this selection of samples is appropriate for the following discussion.

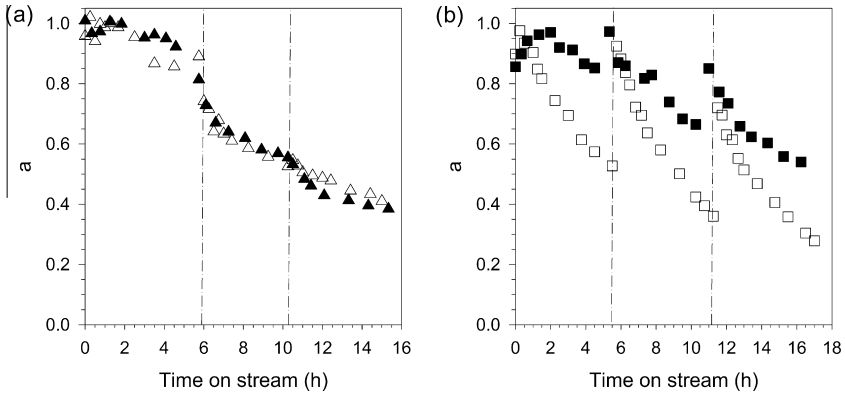

Fig. 3. Comparison of hydrogenation activity of Ru supported on (a) SiO_2 and (b) γ-Al_2O_3. Open symbols represent LA hydrogenation rates. Filled symbols represent 2-pentanone hydrogenation rates.

Table 3
Comparison of physical and chemical characterization of catalyst samples in fresh and spent states. The table also summarizes the percentage of initial activity that was lost irreversibly during the indicated period on stream.

Sample	TOS (h)	Irr. loss (%)	BET (m^2/g)		BJH (nm)		CO uptake (μmol/g)		$d_{p,TEM}$ (nm)[a]	
			Pre	Post	Pre	Post	Pre	Post	Pre	Post
Ru/γ-Al_2O_3	17	17	230	295	5.7	6.9	105	85	1.7 ± 0.1	2.1 ± 0.2
Ru/TiO_2	16	33	55	48	24.1	27.4	15	9	3.1 ± 0.3	5.1 ± 1.2
Ru/SiO_2-A	15	47	468	456	5.5	5.5	116	40	2.7 ± 0.1	5.1 ± 0.4
Ru/C-B	25	87	780	770	5.1	5.0	61	11	4.0 ± 0.3	7.3 ± 0.6

[a] Confidence intervals calculated at 95%.

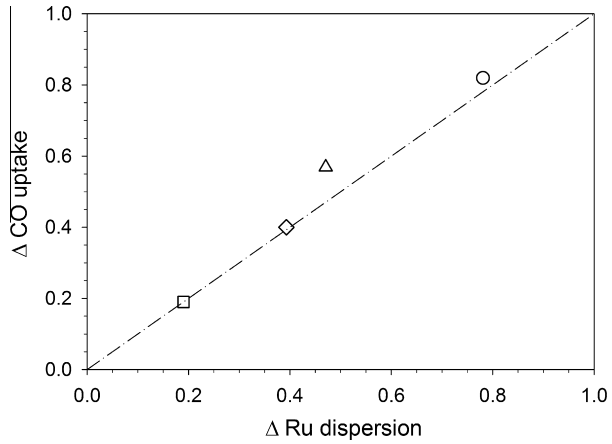

Fig. 4. Loss in irreversible CO uptake in comparison with the change in Ru dispersion estimated from the extent of particle growth. Line of parity indicated by dashed line. (◇) Ru/TiO_2, (○) Ru/C-B, (Δ) Ru/SiO_2-A, and (□) Ru/γ-Al_2O_3. Initial particle diameters for Ru/TiO_2, Ru/SiO_2, and Ru/γ-Al_2O_3 were determined by TEM, and the initial particle diameter of Ru/C-B was calculated from irreversible CO uptake. All final particle diameters were determined by TEM.

samples agree well with dispersion losses calculated based on average particle diameters. We therefore conclude that metal particle growth, as opposed to poison or coke deposition, is the primary source of irreversible deactivation in this system. Although sintering of noble metal particles under reducing environments is typically considered a high-temperature phenomenon [62], this is generally true only for gas-phase treatments. In a bulk condensed phase—especially in water—metal nanoparticles have been demonstrated to sinter under mild conditions [26,30,40,46,63–65]. Thus, despite the low temperature employed in this study, Ru particle growth is a realistic concern. It occurs rapidly, and it contributes substantially to irrecoverable activity losses during aqueous-phase ketone hydrogenation.

The extent of sintering in the period on stream varies considerably between supports, and our results suggest that particle growth is least severe on γ-Al_2O_3 and occurs to larger extents on SiO_2, TiO_2, and C (Table 3). Since initial catalyst preparations differ in particle size, onstream periods vary between samples, and we did not determine equilibrium particle size distributions, it is difficult to make a rigorous determination of whether the supports tested offer varying degrees of "sinter resistance" in aqueous media. Nevertheless, over relatively short times on stream, rates of irreversible deactivation appear first order for all samples

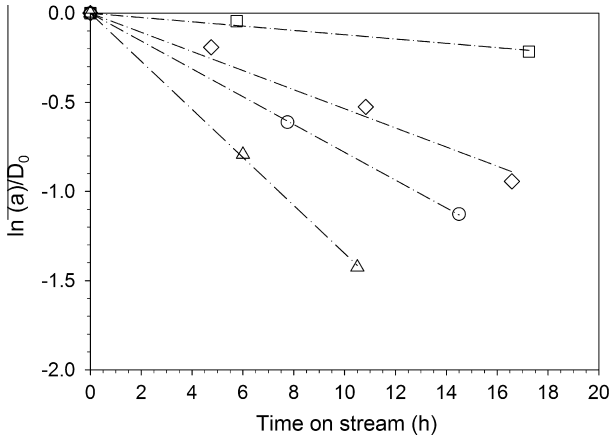

Fig. 5. Illustration of first-order (irreversible) decay in activity with time on stream for Ru supported on (Δ) Ru/SiO_2-A, (○) Ru/C-B, (◇) Ru/TiO_2, and (□) Ru/γ-Al_2O_3. Here, irreversible losses are attributed to particle sintering.

(Fig. 5), and we can make an empirical comparison of sintering kinetics on each support. Assuming that the rate of sintering scales directly with metal dispersion, irreversible deactivation can be modeled using Eq. (5).

$$\left(\frac{da}{dt}\right)_{irr} = -k_s \cdot D \tag{5}$$

Here, a is the catalyst activity defined as its rate of hydrogenation at a given time normalized by its rate of hydrogenation at zero time, k_s is a rate constant that captures sintering kinetics, and D is the metal dispersion at a given time on stream. Since this analysis considers only irreversible activity losses attributed to sintering, and hydrogenation rates should scale linearly with metal dispersion, one may assume that the current activity of a catalyst is given by the ratio of D/D_0, where D_0 is the metal dispersion of the pristine catalyst calculated from irreversible CO uptake. Solution of the resulting differential equation yields Eq. (6), which captures the observed first-order decay in activity. Importantly, this treatment empirically corrects for differences in initial metal dispersion such that sintering kinetics can be quantitatively discussed for all samples despite variation in initial Ru particle size.

$$\ln(a)_{irr} = -k_s \cdot D_0 \cdot t \tag{6}$$

Irreversible activity losses during LA hydrogenation were determined from initial hydrogenation rates measured after each catalyst regeneration shown in Fig. 2. From these data, sintering constants were estimated via least squares regression using the model given by Eq. (6). Model fits are illustrated as dashed lines in Fig. 5, and parameter estimates are given in Table 4. For comparison, sintering constants estimated from irreversible activity losses during 2-pentanone hydrogenation over Ru/γ-Al_2O_3 and Ru/SiO_2-A are additionally included in Table 4.

Considering entries 1, 3, 5, and 6, it is evident that the rate of Ru particle sintering during aqueous-phase ketone hydrogenation varies with the support, decreasing in the order $SiO_2 > C \sim TiO_2 > \gamma$-$Al_2O_3$. Comparison of sintering constants estimated during LA and 2-pentanone hydrogenation over Ru/γ-Al_2O_3 (Entries 1 and 2) and Ru/SiO_2 (Entries 3 and 4) reveals that, for a given support, sintering rates are nearly identical. This suggests that particle growth is not exacerbated by acidity or interactions with LA (at 0.5 M); rather, it appears to be driven by the presence of liquid water and governed by the support. Consistent with observations from high-temperature treatments in H_2, γ-Al_2O_3 provides the best retention of initial metal dispersion while particles supported on SiO_2 appear most sinter prone [62,66].

3.4. Reversible deactivation

Fig. 6 illustrates the extent of reversible deactivation in each system as a function of time on stream. Reversible deactivation profiles were generated by correcting activity profiles shown in Figs. 2 and 3 for irreversible deactivation using Eq. (7), which is based upon a first-order sintering model, and kinetic parameters summarized in Table 4.

Table 4
Estimated sintering constants for various supported Ru catalysts at 90% confidence level.

Entry	Sample	Ketone	k_s (min^{-1})
1	Ru/γ-Al_2O_3	LA	0.72 ± 0.18
2	Ru/γ-Al_2O_3	2-Pentanone	0.74 ± 0.67
3	Ru/SiO_2-A	LA	8.09 ± 0.20
4	Ru/SiO_2-A	2-Pentanone	8.47 ± 1.87
5	Ru/TiO_2	LA	3.21 ± 0.40
6	Ru/C-B	LA	4.44 ± 0.15

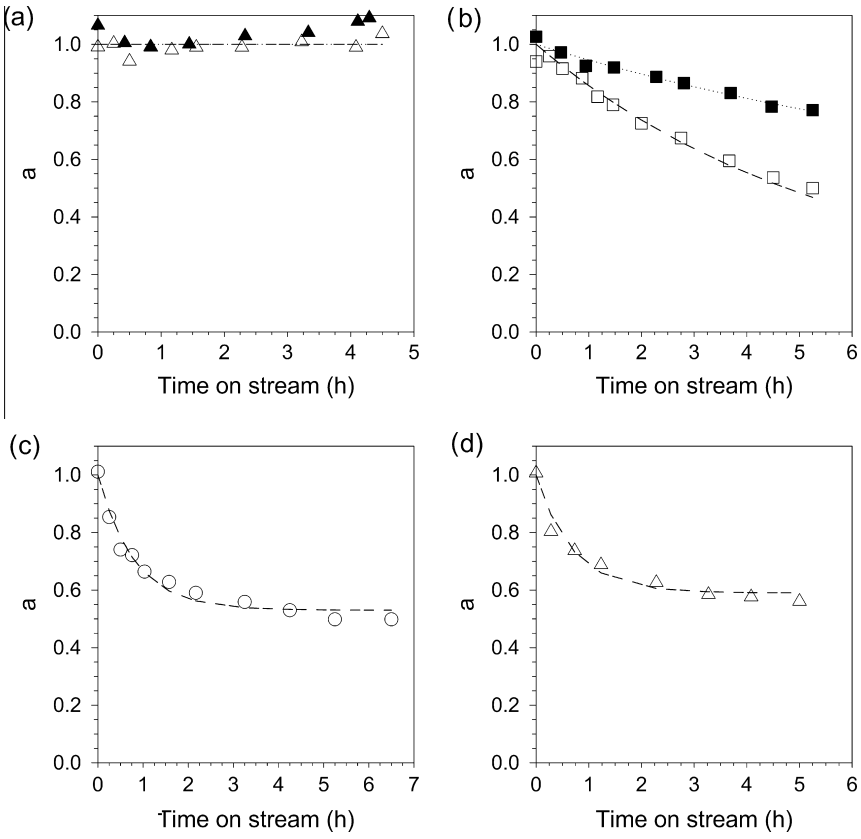

Fig. 6. Profiles of reversible activity loss with time on stream observed for (a) Ru/SiO_2-A, (b) Ru/γ-Al_2O_3, (c) Ru/C-B, and (d) Ru/TiO_2. Open symbols represent rates of LA hydrogenation. Filled symbols represent rates of 2-pentanone hydrogenation. Reversible deactivation profiles were obtained by correcting activity profiles shown in Figs. 2 and 3 for irreversible deactivation due to particle sintering.

$$\ln(a_{rev}) = \ln(a_{overall}) - k_s \cdot D_0 \cdot t \quad (7)$$

As observed for sintering, the extent of reversible deactivation during LA hydrogenation over Ru varies with the identity of the support. At the extremes, Ru/SiO_2 displays no quantifiable reversible deactivation (Fig. 6a), whereas the activity of Ru/γ-Al_2O_3 reversibly decays to 50% of its initial value within 5 h on stream under identical conditions (Fig 6b). Interestingly, the extent of reversible deactivation further varies with the nature of the ketone. For example, reversible deactivation is not observed during either 2-pentanone hydrogenation or LA hydrogenation over Ru/SiO_2 (Fig 6a). In contrast, the difference in reversible activity loss for the analogous experiments over Ru/γ-Al_2O_3 is considerable (Fig 6b). These observations suggest that reversible deactivation is tied both to the identity of the support and to the presence of the carboxylic acid functionality of LA.

Reversible deactivation profiles are captured by a first-order model (Eq. (8)) that allows for activity to approach a nonzero steady state value.

$$\frac{da_{rev}}{dt} = -k_{rev} \cdot (a_{rev} - a_\infty) \quad (8)$$

This model provides two variable parameters that capture the kinetic approach to steady state (k_{rev}) and the activity remaining at steady state (a_∞). Optimal parameter estimates for Ru/γ-Al_2O_3, Ru/TiO_2, and Ru/C are summarized in Table 5, and their values were used to generate model fits illustrated in Fig. 6. Ru/SiO_2 displayed no quantifiable reversible deactivation during either LA or 2-pentanone hydrogenation, and parameter values were accordingly not estimated for these systems. Reversible deactivation occurs quickly relative to sintering, which is indicated by first-order decay constants that are generally an order of magnitude larger than sintering constants given in Table 4. Further, the extent of reversible deactivation during LA hydrogenation, indicated by the value of a_∞, decreases with support identity in the order $Al_2O_3 > C \sim TiO_2 > SiO_2$.

Table 5
Summary of estimated reversible deactivation parameters during the hydrogenation of LA and 2-pentanone over Ru on various supports.

Sample	Ketone	k_{rev} (min^{-1})	a_∞[a]
Ru/SiO_2-A	LA	0	1.0
Ru/γ-Al_2O_3	LA	11	0.13 ± 0.35
Ru/TiO_2	LA	86	0.59 ± 0.05
Ru/C-B	LA	74	0.53 ± 0.03
Ru/SiO_2-A	2-pentanone	0	1.0
Ru/γ-Al_2O_3	2-pentanone	6	0.43 ± 0.79

[a] Calculated at 95% confidence level.

Given that Ru/γ-Al_2O_3 exhibits more pronounced (reversible) deactivation during LA hydrogenation than it does during 2-pentanone hydrogenation, it appears that carboxylic acids exacerbate this mode of instability. To further probe this, the onstream stability of Ru/γ-Al_2O_3 was monitored during 2-pentanone hydrogenation at 323 K and 24 bar H_2 in the presence of propanoic acid (0.5 M, pH = 2.59). The results of this experiment are presented in Fig. 7. Whereas Ru/γ-Al_2O_3 is relatively stable during 2-pentanone hydrogenation (Fig. 2), it deactivates rapidly in the presence of 0.5 M propanoic acid (Fig. 7). During this experiment, 2-pentanol was the only hydrogenation product observed; no propanoic acid hydrogenation products were detected by GC–MS. Upon removal of propanoic acid, the rate of 2-pentanone hydrogenation improves, returning to 54% of the original activity within 2 h. The

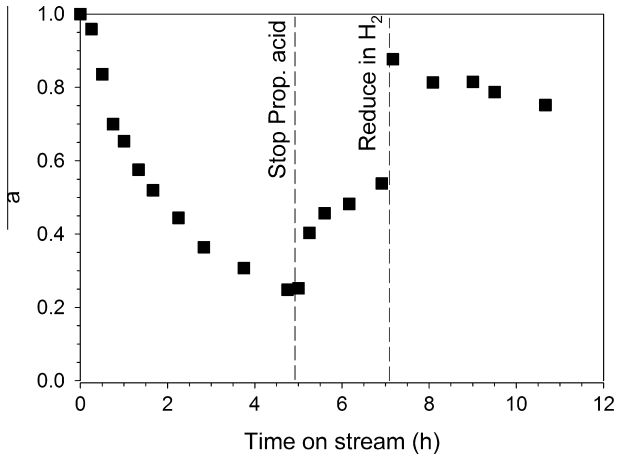

Fig. 7. Activity profile of Ru/γ-Al_2O_3 during the hydrogenation of 2-pentanone in the presence of propanoic acid.

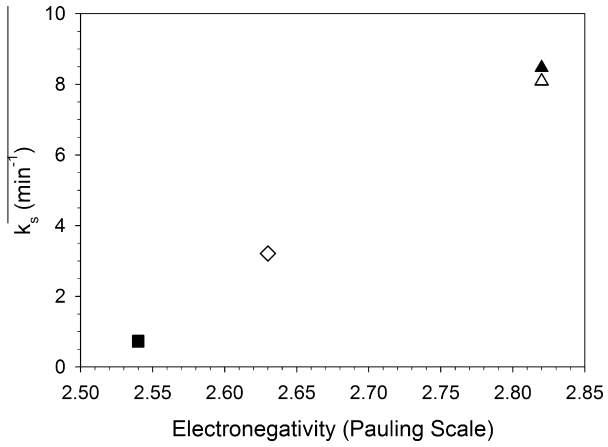

Fig. 8. Correlation between sintering constants and electronegativity of a bulk oxide. (◇) Ru/TiO_2, (Δ) Ru/SiO_2-A, and (□) Ru/γ-Al_2O_3. Open symbols represent sintering rates during LA hydrogenation. Filled symbols represent sintering rates during 2-pentanone hydrogenation.

aqueous flow was then stopped, and the catalyst was left under H_2 (100 ml min^{-1}, 323 K, 15 h) to evaluate the extent of reversibility. Upon reintroducing an aqueous, acid-free 2-pentanone feed, the catalyst achieved 88% of its initial activity, with the 12% irrecoverable loss attributed to sintering. Using parameters summarized in Table 4, we estimate that, in water, our fresh Ru/γ-Al_2O_3 sample should lose 5–10% of its metal surface area to sintering during its first 7 h on stream, which agrees with the 12% irreversible loss in activity observed here.

4. Discussion

Results summarized in the preceding sections demonstrate that Ru nanoparticles supported on various carbons and solid oxides display comparable intrinsic activity toward aqueous-phase ketone hydrogenation but are susceptible to varying extents of irreversible and reversible deactivation. The former is support-dependent and attributed to particle sintering, which is accelerated in bulk water relative to bulk gas phases. The mechanism of the latter is unclear, but its severity depends both on the nature of the support and the presence of carboxylic acids.

With respect to sintering, γ-Al_2O_3 appears to stabilize Ru dispersion in water relatively well compared to SiO_2, TiO_2, and C. Electronegativity has been previously employed to explain different sintering extents on various supports [66,67], and we build on this argument here. M-O-Ru bonds, in which M is the support cation (Si^{4+}, Ti^{4+}, or Al^{3+}), change character with the nature of M. Specifically, as support cations become increasingly electronegative (e.g., Si^{4+}), the electron density on the oxygen is decreased, and one may expect less favorable M-O-Ru interactions. In contrast, for support cations with relatively low electronegativities (e.g., Ti^{4+}, Al^{3+}), the oxygen of the M-O-Ru bond should have a relatively high electron density, and one may expect more favorable Ru–support interactions. Our data generally agree with this interpretation; however, instead of relating particle sintering to cation electronegativity, we observe a stronger correlation with the mean electronegativity of the bulk oxide, which can be calculated as the geometric mean of the electronegativity of the metal cation and oxygen in the oxide lattice according to Eq. (9) [68]:

$$\chi_{M_xO_y} = [\chi_M^x \cdot \chi_O^y]^{\frac{1}{x+y}} \quad (9)$$

In Eq. (9), χ_j is the electronegativity of a given species. As illustrated in Fig. 8 for γ-Al_2O_3, TiO_2, and SiO_2, we observe that sintering constants increase as the mean electronegativity of the oxide increases. Based on this correlation, we interpret sinter resistance in the context of hard–soft acid–base theory. Specifically, solid oxides with low electronegativities (e.g., γ-Al_2O_3, TiO_2) can be considered relatively soft bases whereas those with high electronegativity (e.g., SiO_2) may be classified as relatively hard bases. Low-valent Ru is considered a relatively soft acid [69], and it stands to reason that its interactions are more favorable with supports that are softer bases. According to this interpretation, the severity of sintering should decrease on oxide supports in the order SiO_2 > TiO_2 > γ-Al_2O_3, which is consistent with our observations. Because of its surface heterogeneity, it is difficult to include carbon in a discussion based on support electronegativity; however, the insight that Ru particle stability correlates with electron density of a support surface could aid in developing a sinter-resistant carbon support, provided that the surface functionality of carbon can be controlled during catalyst synthesis and retained under reaction conditions.

Based on the experimental evidence presented here, we cannot conclusively define a mechanism for reversible deactivation; nonetheless, it is worth examining potential causes. Because activity not lost through sintering can be restored by reductive treatment—although not through thermal treatment in an inert atmosphere—it stands to reason that this mode of deactivation is oxidative in nature. Further, as demonstrated in Fig. 7, carboxylic acids exacerbate reversible deactivation, suggesting that system pH or carboxylate adsorption may underlie the phenomena. Based on measured turnover frequencies and residence times, we anticipate the reported systems should reach steady state on the scale of minutes, yet we observe that hydrogenation activity continues to decay (reversibly) on the scale of hours.

Considering oxidative phenomena in a bulk aqueous phase, it is possible that water dissociation could result in the formation of bound hydroxyls on Ru surfaces. Surface hydroxyls should be removed by reduction in dry H_2, restoring Ru sites to their metallic state. However, one would typically expect adsorption processes to equilibrate quickly such that competitive binding should manifest as a diminished steady state hydrogenation rate rather than a transient decay in hydrogenation rate. Surface science experiments have suggested that dissociative adsorption of water on Ru is an activated process [70,71]. It is thus possible that water dissociation occurs slowly relative to the adsorption of reactive species such that hydroxyl coverages equilibrate on relatively longtime scales, which might explain the gradual decrease in activity with time on stream.

Although surface oxidation via hydroxyl binding is potentially consistent with observed activity profiles, prior reports argue against Ru oxidation under our experimental conditions. Based on a redox potential of −0.5 to −0.7 V for H_2 saturated water [8], Pourbaix diagrams suggest that bulk Ru in aqueous solution is metallic at any pH [72]. Further, Davis has employed in situ X-ray absorption spectroscopy to conclude that Ru is zerovalent in H_2 saturated water at 373 K, and that it remains fully reduced upon exposure to N_2 saturated water at the same temperature [26]. That said, the above results are most applicable to bulk Ru metal and perhaps less so to Ru surfaces. Without a surface sensitive in situ characterization method (e.g., XPS), it is not possible to either confirm or eliminate oxidation of Ru surface sites as a source of reversible deactivation in this system.

Reversible deactivation during LA hydrogenation is most severe on the least electronegative oxide (γ-Al_2O_3) and not detected on the most electronegative oxide (SiO_2). Thus, in contrast to sintering, reversible deactivation appears to correlate inversely with mean oxide electronegativity. Another property of solid oxides that scales in this fashion is their point of zero charge (PZC) in aqueous media, and our observations are interpreted further on this basis. Taken relative to solution pH, the PZC of a material is a predictor of its net surface charge [73]. If a material is suspended in a solution that has a pH above its PZC, that material's surface should be, on average, negatively charged. In contrast, if a material is employed in a solution that has a pH below its PZC, that material's surface should be positively charged [74]. Furthermore, as the magnitude of the gap between PZC and solution pH increases, |PZC-pH|, so does the deviation from a net zero surface charge. PZCs for the supports employed here are summarized in Table 6. Values for SiO_2, γ-Al_2O_3, and TiO_2 were taken from reference data [75], and the value for C was measured using an equilibrium-based mass titration method [38].

Under the LA hydrogenation conditions in this study, the initial pH of the aqueous phase was measured at 2.45. At this pH, SiO_2 should have a net negative surface charge, and all other supports should be positively charged. Interestingly, we observe only irreversible deactivation in Ru/SiO_2, whereas some portion of the deactivation is always reversible in the remaining three catalysts. These observations suggest that, when supported on positively charged surfaces, Ru will exhibit reversible deactivation during ketone hydrogenation in the presence of carboxylic acids. Moreover, γ-Al_2O_3 should have a high density of positive surface charges relative to, e.g., TiO_2, indicating that the severity of reversible deactivation scales with increasing positive surface charge. This correlation, along with its connection to solution pH and a material's PZC, is illustrated in Fig. 9.

A potential explanation is that carboxylate anions present in solution bind favorably to positively charged supports and less so to negatively charged supports. This argument, applied to ionic metal complexes, underlies the strong electrostatic adsorption method of catalyst synthesis [76], and should extend to carboxylate anions under reaction conditions. Accordingly, one might expect high carboxylate coverage on γ-Al_2O_3 while the surface of SiO_2 remains relatively carboxylate-free under identical conditions. It is unlikely that variation in carboxylate coverage on the support should impact the carboxylate coverage on Ru particles, which will ultimately reflect equilibrium with the bulk. That said, it may be possible that ketone and/or H_2 coordination at Ru sites become increasingly hindered on carboxylate covered supports. If so, one might expect that interfacial sites—and thus smaller Ru particles, such as those as observed on γ-Al_2O_3—would be particularly susceptible to this mode of "site blocking."

Table 6
Summary of PZC values of the various supports employed.

Sample	PZC
Ru/SiO_2-A	1.8
Ru/γ-Al_2O_3	8.8
Ru/TiO_2	6.3
Ru/C-B	6.6

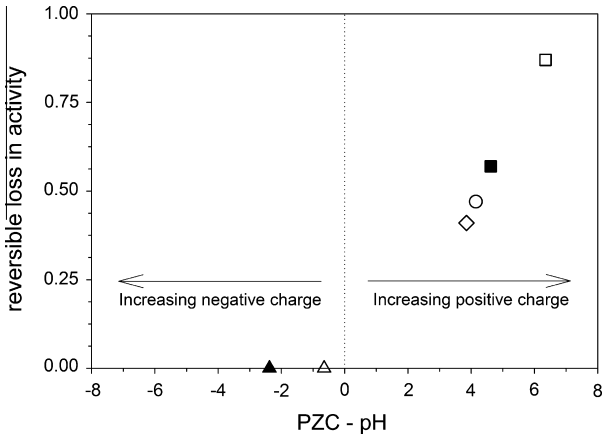

Fig. 9. Correlation between PZC (and surface charge) with the extent of reversible deactivation on each Ru–support combination considered during the hydrogenation of levulinic acid and 2-pentanone. (◇) Ru/TiO_2, (○) Ru/C-B, (△) Ru/SiO_2-A, and (□) Ru/γ-Al_2O_3. Open symbols represent reversible losses during LA hydrogenation. Filled symbols represent reversible losses during 2-pentanone hydrogenation.

5. Conclusion

The activity and stability of Ru nanoparticles during the aqueous-phase hydrogenation of LA and 2-pentanone was studied across various supports. The intrinsic rate of hydrogenation was found to be invariant with support identity and particle size, indicating a structure insensitive reaction and no strong metal—support interactions. Comparable rates of LA and 2-pentanone hydrogenation show that the secondary carboxylic functionality of LA does not perturb the intrinsic rate of ketone hydrogenation over Ru surfaces in water. Deactivation of Ru nanoparticles occurs through reversible and irreversible phenomena, both of which appear to be governed by the mean electronegativity of the support. The irreversible loss in activity is attributed to the sintering of Ru nanoparticles, and it increases in severity with the electronegativity of the support. The source of reversible deactivation could not be conclusively identified; however, it is both support- and carboxylic acid-dependent, and its extent appears to scale with the prevailing surface charge of the support. Hydrogenation of carboxylic acids in water is unique in that the reaction media comprises an electrolyte solution. It stands to reason that electrostatic interactions between dissociated ions and charged surfaces may influence catalyst stability; however, broader consideration of support systems and reaction media is necessary to substantiate any such connections.

The experiments summarized here were carried out under continuous flow conditions, and they reveal time- and media-dependent changes in the catalytic activity of Ru sites during aqueous-phase hydrogenations. Aqueous-phase reactions in general and biomass upgrading reactions in particular are most commonly studied in batch vessels, and conclusions regarding catalytic activity are frequently drawn from time-dependent reactor balances and ex situ characterization methods (e.g., chemisorption). In systems, such as this one, where the catalyst undergoes pronounced structure and/or activity changes on timescales that are comparable to the duration of a typical experiment, rigorous

analysis of batch kinetic data is challenging, and it can be difficult to estimate meaningful turnover frequencies from such experiments. Here, we have addressed this issue through estimation of initial rates, but the approach is time consuming and imprecise relative to acquisition of steady state rate data. Reliable, experimental determination of site-specific rates in aqueous-phase systems would benefit from the development of an accessible, operando method for active site titration and/or structural analysis under aqueous-phase reaction conditions.

With respect to catalyst design, our observations suggest that multiple aspects of aqueous-phase stability are influenced by the electronegativity of the support. Unfortunately, these dependencies appear varied in nature, and tension may exist between, e.g., stabilizing against sintering and stabilizing against reversible deactivation. Although we are not presently able to envision a single Ru–support combination that might satisfy all stability criteria, insights into governing phenomena are useful. For example, composite materials that have distinct, well-defined domains of varying electronegativity may be a compelling choice of support for Ru when it is employed in aqueous media [77]. Further, we emphasize the significance of efforts to stabilize metal dispersion through *physical* encapsulation of nanoclusters using, for example, atomic layer deposition [78–80]. Such approaches may allow one to decouple reversible and irreversible modes of deactivation and thus design a truly resilient catalyst for use in harsh media. With respect to support selection, it is important to mention that, although we have used solid oxides here to probe fundamental aspects of activity and stability, they are unlikely to be suitable supports under all reaction conditions. For aqueous-phase processes, complexity is added by the fact that one must additionally ensure that support integrity is maintained at high temperatures and pressures.

Acknowledgments

OAA, JQB, and AH acknowledge financial support for this work from the National Science Foundation – United States (CBET, Award Number 1159739). HYL and YRL acknowledge financial support for this work from the U.S. Department of Energy, Office of Science, Office of Basic Energy Sciences, Chemical Sciences, Geosciences and Biosciences Division under Grant No. DE-FG02-12ER16352.

Appendix A. Supplementary material

Supplementary data associated with this article can be found, in the online version, at http://dx.doi.org/10.1016/j.jcat.2015.04.026.

References

[1] J.W. Shabaker, G.W. Huber, J.A. Dumesic, Aqueous-phase reforming of oxygenated hydrocarbons over Sn-modified Ni catalysts, J. Catal. 222 (2004) 180–191.
[2] R.D. Cortright, R.R. Davda, J.A. Dumesic, Hydrogen from catalytic reforming of biomass-derived hydrocarbons in liquid water, Nature 418 (2002) 964–967.
[3] J.A. Lopez-Ruiz, R.J. Davis, Decarbonylation of heptanoic acid over carbon-supported platinum nanoparticles, Green Chem. 16 (2014) 683–694.
[4] J.Q. Bond, D. Wang, D.M. Alonso, J.A. Dumesic, Interconversion between γ-valerolactone and pentenoic acid combined with decarboxylation to form butene over silica/alumina, J. Catal. 281 (2011) 290–299.
[5] A.B. Kellicutt, R. Salary, O.A. Abdelrahman, J.Q. Bond, An examination of the intrinsic activity and stability of various solid acids during the catalytic decarboxylation of [gamma]-valerolactone, Catal. Sci. Technol. 4 (2014) 2267–2279.
[6] D. Wang, S.H. Hakim, D. Martin Alonso, J.A. Dumesic, A highly selective route to linear alpha olefins from biomass-derived lactones and unsaturated acids, Chem. Commun. 49 (2013) 7040–7042.
[7] M. Snåre, I. Kubičková, P. Mäki-Arvela, K. Eränen, D.Y. Murzin, Heterogeneous catalytic deoxygenation of stearic acid for production of biodiesel, Ind. Eng. Chem. Res. 45 (2006) 5708–5715.
[8] I.M. Piskarev, V.A. Ushkanov, N.A. Aristova, P.P. Likhachev, T.S. Myslivets, Establishment of the redox potential of water saturated with hydrogen, Biophysics 55 (2010) 13–17.
[9] R.M. West, Z.Y. Liu, M. Peter, J.A. Dumesic, Liquid alkanes with targeted molecular weights from biomass-derived carbohydrates, ChemSusChem 1 (2008) 417–424.
[10] B.M. Moreno, N. Li, J. Lee, G.W. Huber, M.T. Klein, Modeling aqueous-phase hydrodeoxygenation of sorbitol over Pt/SiO_2-Al_2O_3, RSC Adv. 3 (2013) 23769–23784.
[11] G.W. Huber, J.N. Chheda, C.J. Barrett, J.A. Dumesic, Production of liquid alkanes by aqueous-phase processing of biomass-derived carbohydrates, Science 308 (2005) 1446–1450.
[12] G.W. Huber, J.W. Shabaker, S.T. Evans, J.A. Dumesic, Aqueous-phase reforming of ethylene glycol over supported Pt and Pd bimetallic catalysts, Appl. Catal. B 62 (2006) 226–235.
[13] E.L. Kunkes, D.A. Simonetti, J.A. Dumesic, W.D. Pyrz, L.E. Murillo, J.G. Chen, D.J. Buttrey, The role of rhenium in the conversion of glycerol to synthesis gas over carbon supported platinum–rhenium catalysts, J. Catal. 260 (2008) 164–177.
[14] J.W. Shabaker, R.R. Davda, G.W. Huber, R.D. Cortright, J.A. Dumesic, Aqueous-phase reforming of methanol and ethylene glycol over alumina-supported platinum catalysts, J. Catal. 215 (2003) 344–352.
[15] T. van Haasterecht, C.C.I. Ludding, K.P. de Jong, J.H. Bitter, Toward stable nickel catalysts for aqueous phase reforming of biomass-derived feedstock under reducing and alkaline conditions, J. Catal. 319 (2014) 27–35.
[16] H.Y. Luo, D.F. Consoli, W.R. Gunther, Y. Román-Leshkov, Investigation of the reaction kinetics of isolated Lewis acid sites in Beta zeolites for the Meerwein–Ponndorf–Verley reduction of methyl levulinate to γ-valerolactone, J. Catal. 320 (2014) 198–207.
[17] M. Chia, J.A. Dumesic, Liquid-phase catalytic transfer hydrogenation and cyclization of levulinic acid and its esters to [gamma]-valerolactone over metal oxide catalysts, Chem. Commun. 47 (2011) 12233–12235.
[18] J. Jae, E. Mahmoud, R.F. Lobo, D.G. Vlachos, Cascade of liquid-phase catalytic transfer hydrogenation and etherification of 5-hydroxymethylfurfural to potential biodiesel components over lewis acid zeolites, ChemCatChem 6 (2014) 508–513.
[19] J.D. Lewis, S. Van de Vyver, A.J. Crisci, W.R. Gunther, V.K. Michaelis, R.G. Griffin, Y. Román-Leshkov, A continuous flow strategy for the coupled transfer hydrogenation and etherification of 5-(hydroxymethyl)furfural using lewis acid zeolites, ChemSusChem 7 (2014) 2255–2265.
[20] L. Bui, H. Luo, W.R. Gunther, Y. Román-Leshkov, Domino reaction catalyzed by zeolites with brønsted and lewis acid sites for the production of γ-valerolactone from furfural, Angew. Chem. Int. Ed. 52 (2013) 8022–8025.
[21] O.A. Abdelrahman, A. Heyden, J.Q. Bond, Analysis of kinetics and reaction pathways in the aqueous-phase hydrogenation of levulinic acid to form γ-valerolactone over RU/C, ACS Catal. 4 (2014) 1171–1181.
[22] L.E. Manzer, Catalytic synthesis of alpha-methylene-gamma-valerolactone: a biomass-derived acrylic monomer, Appl. Catal. A 272 (2004) 249–256.
[23] Z.J. Wu, S.H. Ge, C.X. Ren, M.H. Zhang, A. Yip, C.M. Xu, Selective conversion of cellulose into bulk chemicals over Bronsted acid-promoted ruthenium catalyst: one-pot vs. sequential process, Green Chem. 14 (2012) 3336–3343.
[24] L. Deng, Y. Zhao, J.A. Li, Y. Fu, B. Liao, Q.X. Guo, Conversion of levulinic acid and formic acid into gamma-valerolactone over heterogeneous catalysts, ChemSusChem 3 (2010) 1172–1175.
[25] R. Luque, J.H. Clark, Water-tolerant Ru-Starbon (R) materials for the hydrogenation of organic acids in aqueous ethanol, Catal. Commun. 11 (2010) 928–931.
[26] E.P. Maris, W.C. Ketchie, O. Vladimir, R.J. Davis, Metal particle growth during glucose hydrogenation over Ru/SiO_2 evaluated by X-ray absorption spectroscopy and electron microscopy, J. Phys. Chem. B 110 (2006) 7869–7876.
[27] B.J. Arena, Deactivation of ruthenium catalysts in continuous glucose hydrogenation, Appl. Catal. A 87 (1992) 219–229.
[28] K. Yan, J. Liao, X. Wu, X. Xie, A noble-metal free Cu-catalyst derived from hydrotalcite for highly efficient hydrogenation of biomass-derived furfural and levulinic acid, RSC Adv. 3 (2013) 3853–3856.
[29] A.M. Hengne, C.V. Rode, $Cu–ZrO_2$ nanocomposite catalyst for selective hydrogenation of levulinic acid and its ester to [gamma]-valerolactone, Green Chem. 14 (2012) 1064–1072.
[30] Y. Wang, S. Van de Vyver, K.K. Sharma, Y. Roman-Leshkov, Insights into the stability of gold nanoparticles supported on metal oxides for the base-free oxidation of glucose to gluconic acid, Green Chem. 16 (2014) 719–726.
[31] D.J. Braden, C.A. Henao, J. Heltzel, C.C. Maravelias, J.A. Dumesic, Production of liquid hydrocarbon fuels by catalytic conversion of biomass-derived levulinic acid, Green Chem. 13 (2011) 1755–1765.
[32] J.Q. Bond, A.A. Upadhye, H. Olcay, G.A. Tompsett, J. Jae, R. Xing, D.M. Alonso, D. Wang, T. Zhang, R. Kumar, A. Foster, S.M. Sen, C.T. Maravelias, R. Malina, S.R.H. Barrett, R. Lobo, C.E. Wyman, J.A. Dumesic, G.W. Huber, Production of renewable jet fuel range alkanes and commodity chemicals from integrated catalytic processing of biomass, Energy Environ. Sci. 7 (2014) 1500–1523.
[33] M.S. Ide, D.D. Falcone, R.J. Davis, On the deactivation of supported platinum catalysts for selective oxidation of alcohols, J. Catal. 311 (2014) 295–305.
[34] R.D. Cortright, M. Sanchez-Castillo, J.A. Dumesic, Conversion of biomass to 1,2-propanediol by selective catalytic hydrogenation of lactic acid over silica-supported copper, Appl. Catal. B 39 (2002) 353–359.
[35] Z. Zhang, J.E. Jackson, D.J. Miller, Aqueous-phase hydrogenation of lactic acid to propylene glycol, Appl. Catal. A 219 (2001) 89–98.

[36] M.A.N. Santiago, M.A. Sánchez-Castillo, R.D. Cortright, J.A. Dumesic, Catalytic reduction of acetic acid, methyl acetate, and ethyl acetate over silica-supported copper, J. Catal. 193 (2000) 16–28.
[37] E.L. Kunkes, D.A. Simonetti, R.M. West, J.C. Serrano-Ruiz, C.A. Gärtner, J.A. Dumesic, Catalytic conversion of biomass to monofunctional hydrocarbons and targeted liquid-fuel classes, Science 322 (2008) 417–421.
[38] A.H. Van Pelt, O.A. Simakova, S.M. Schimming, J.L. Ewbank, G.S. Foo, E.A. Pidko, E.J.M. Hensen, C. Sievers, Stability of functionalized activated carbon in hot liquid water, Carbon 77 (2014) 143–154.
[39] H.N. Pham, A.E. Anderson, R.L. Johnson, K. Schmidt-Rohr, A.K. Datye, Improved hydrothermal stability of mesoporous oxides for reactions in the aqueous phase, Angew. Chem. Int. Ed. 51 (2012) 13163–13167.
[40] W.C. Ketchie, E.P. Maris, R.J. Davis, In-situ X-ray absorption spectroscopy of supported Ru catalysts in the aqueous phase, Chem. Mater. 19 (2007) 3406–3411.
[41] H. Xiong, H.N. Pham, A.K. Datye, Hydrothermally stable heterogeneous catalysts for conversion of biorenewables, Green Chem. 16 (2014) 4627–4643.
[42] H. Xiong, H.N. Pham, A.K. Datye, A facile approach for the synthesis of niobia/carbon composites having improved hydrothermal stability for aqueous-phase reactions, J. Catal. 302 (2013) 93–100.
[43] W. Luo, M. Sankar, A.M. Beale, Q. He, C.J. Kiely, P.C.A. Bruijnincx, B.M. Weckhuysen, High performing and stable supported nano-alloys for the catalytic hydrogenation of levulinic acid to γ-valerolactone, Nat. Commun. 6 (2015).
[44] S.G. Wettstein, J.Q. Bond, D.M. Alonso, H.N. Pham, A.K. Datye, J.A. Dumesic, RuSn bimetallic catalysts for selective hydrogenation of levulinic acid to γ-valerolactone, Appl. Catal. B 117–118 (2012) 321–329.
[45] S. Lowell, Characterization of Porous Solids and Powders: Surface Area, Pore Size and Density, Springer, 2004.
[46] J.H. Vleeming, B.F.M. Kuster, G.B. Marin, F. Oudet, P. Courtine, Graphite-supported platinum catalysts: effects of gas and aqueous phase treatments, J. Catal. 166 (1997) 148–159.
[47] P. Reyes, M.E. König, G. Pecchi, I. Concha, M. López Granados, J.L.G. Fierro, O-xylene hydrogenation on supported ruthenium catalysts, Catal. Lett. 46 (1997) 71–75.
[48] G. Neri, L. Mercadante, A. Donato, A.M. Visco, S. Galvagno, Influence of Ru precursor, support and solvent in the hydrogenation of citral over ruthenium catalysts, Catal. Lett. 29 (1994) 379–386.
[49] A. Basińska, L. Kępiński, F. Domka, The effect of support on WGSR activity of ruthenium catalysts, Appl. Catal. A 183 (1999) 143–153.
[50] N.V. Pavlenko, A.I. Tripol'skii, G.I. Golodets, Vapor-phase hydrogenation of acetone on applied metals of the platinum group, Theor. Exp. Chem. 22 (1987) 667–675.
[51] B. Sen, M.A. Vannice, Metal-support effects on acetone hydrogenation over platinum catalysts, J. Catal. 113 (1988) 52–71.
[52] F. Rositani, S. Galvagno, Z. Poltarzewski, P. Staiti, P.L. Antonucci, Kinetics of acetone hydrogenation over Pt/Al_2O_3 catalysts, J. Chem. Technol. Biotechnol. 35 (1985) 234–240.
[53] H. Wan, A. Vitter, R.V. Chaudhari, B. Subramaniam, Kinetic investigations of unusual solvent effects during Ru/C catalyzed hydrogenation of model oxygenates, J. Catal. 309 (2014) 174–184.
[54] H.G. Manyar, D. Weber, H. Daly, J.M. Thompson, D.W. Rooney, L.F. Gladden, E. Hugh Stitt, J. Jose Delgado, S. Bernal, C. Hardacre, Deactivation and regeneration of ruthenium on silica in the liquid-phase hydrogenation of butan-2-one, J. Catal. 265 (2009) 80–88.
[55] R.J. Madon, M. Boudart, Experimental criterion for the absence of artifacts in the measurement of rates of heterogeneous catalytic reactions, Ind. Eng. Chem. Fundam. 21 (1982) 438–447.
[56] R.M. Koros, E.J. Nowak, A diagnostic test of the kinetic regime in a packed bed reactor, Chem. Eng. Sci. 22 (1967) 470.
[57] S.J. Tauster, Strong metal-support interactions, Acc. Chem. Res. 20 (1987) 389–394.
[58] S.J. Tauster, S.C. Fung, R.L. Garten, Strong metal-support interactions. Group 8 noble metals supported on titanium dioxide, JACS 100 (1978) 170–175.
[59] G. Lefèvre, M. Duc, P. Lepeut, R. Caplain, M. Fédoroff, Hydration of γ-alumina in water and its effects on surface reactivity, Langmuir 18 (2002) 7530–7537.
[60] J. Duan, Y.T. Kim, H. Lou, G.W. Huber, Hydrothermally stable regenerable catalytic supports for aqueous-phase conversion of biomass, Catal. Today 234 (2014) 66–74.
[61] W. Luo, U. Deka, A.M. Beale, E.R.H. van Eck, P.C.A. Bruijnincx, B.M. Weckhuysen, Ruthenium-catalyzed hydrogenation of levulinic acid: influence of the support and solvent on catalyst selectivity and stability, J. Catal. 301 (2013) 175–186.
[62] C.H. Bartholomew, Mechanisms of catalyst deactivation, Appl. Catal. A 212 (2001) 17–60.
[63] A. Douidah, P. Marécot, S. Labruquère, J. Barbier, Stability of supported platinum catalysts in aqueous phase under hydrogen atmosphere, Appl. Catal. A 210 (2001) 111–120.
[64] A. Douidah, P. Marécot, J. Barbier, Toward a better understanding of the stability of supported platinum catalysts in aqueous phase under hydrogen atmosphere at room temperature, Appl. Catal. A 225 (2002) 11–19.
[65] M. Besson, P. Gallezot, Deactivation of metal catalysts in liquid phase organic reactions, Catal. Today 81 (2003) 547–559.
[66] Y. Nagai, T. Hirabayashi, K. Dohmae, N. Takagi, T. Minami, H. Shinjoh, S.I. Matsumoto, Sintering inhibition mechanism of platinum supported on ceria-based oxide and Pt-oxide–support interaction, J. Catal. 242 (2006) 103–109.
[67] K. Asakura, Y. Iwasawa, Surface structure and catalysis for CO hydrogenation of the supported Ru species derived from the $Ru_3(CO)_{12}$ inorganic oxides, J. Chem. Soc., Faraday Trans. 86 (1990) 2657–2662.
[68] M.A. Butler, D.S. Ginley, Prediction of flatband potentials at semiconductor-electrolyte interfaces from atomic electronegativities, J. Electrochem. Soc. 125 (1978) 228–232.
[69] R.G. Pearson, Hard and soft acids and bases, HSAB, part 1: fundamental principles, J. Chem. Educ. 45 (1968) 581.
[70] K. Andersson, A. Gómez, C. Glover, D. Nordlund, H. Öström, T. Schiros, O. Takahashi, H. Ogasawara, L.G.M. Pettersson, A. Nilsson, Molecularly intact and dissociative adsorption of water on clean Cu(1 1 0): a comparison with the water/Ru(0 0 1) system, Surf. Sci. 585 (2005) L183–L189.
[71] K. Andersson, A. Nikitin, L.G.M. Pettersson, A. Nilsson, H. Ogasawara, Water dissociation on Ru(001): an activated process, Phys. Rev. Lett. 93 (2004) 196101.
[72] H. Cui, J.-H. Park, J.-G. Park, Effect of oxidizers on chemical mechanical planarization of ruthenium with colloidal silica based slurry, J. Solid State Sci. Technol. 2 (2013) P26–P30.
[73] M. Kosmulski, The pH-dependent surface charging and the points of zero charge, J. Colloid Interface Sci. 253 (2002) 77–87.
[74] J.S. Noh, J.A. Schwarz, Estimation of the point of zero charge of simple oxides by mass titration, J. Colloid Interface Sci. 130 (1989) 157–164.
[75] I.E. Wachs, Molecular structures of surface metal oxide species: nature of catalytic active sites in mixed metal oxides, in: J.L.G. Fierro (Ed.), Metal Oxides: Chemistry and Applications, Taylor & Francis, 2006, p. 4.
[76] X. Hao, L. Quach, J. Korah, W.A. Spieker, J.R. Regalbuto, The control of platinum impregnation by PZC alteration of oxides and carbon, J. Mol. Catal. A: Chem. 219 (2004) 97–107.
[77] J.E. Samad, S. Hashim, S. Ma, J.R. Regalbuto, Determining surface composition of mixed oxides with pH, J. Colloid Interface Sci. 436 (2014) 204–210.
[78] B.J. O'Neill, D.H.K. Jackson, A.J. Crisci, C.A. Farberow, F. Shi, A.C. Alba-Rubio, J. Lu, P.J. Dietrich, X. Gu, C.L. Marshall, P.C. Stair, J.W. Elam, J.T. Miller, F.H. Ribeiro, P.M. Voyles, J. Greeley, M. Mavrikakis, S.L. Scott, T.F. Kuech, J.A. Dumesic, Stabilization of copper catalysts for liquid-phase reactions by atomic layer deposition, Angew. Chem. 125 (2013) 14053–14057.
[79] A.C. Alba-Rubio, B.J. O'Neill, F. Shi, C. Akatay, C. Canlas, T. Li, R. Winans, J.W. Elam, E.A. Stach, P.M. Voyles, J.A. Dumesic, Pore structure and bifunctional catalyst activity of overlayers applied by atomic layer deposition on copper nanoparticles, ACS Catal. 4 (2014) 1554–1557.
[80] J. Lu, J.W. Elam, P.C. Stair, Synthesis and stabilization of supported metal catalysts by atomic layer deposition, Acc. Chem. Res. 46 (2013) 1806–1815.